




Thermal Wave Instability as an Origin of Gap and Ring Structures in Protoplanetary Disks

Takahiro Ueda¹ , Mario Flock² , and Tilman Birnstiel^{3,4} ¹ National Astronomical Observatory of Japan, Osawa 2-21-1, Mitaka, Tokyo 181-8588, Japan; takahiro.ueda@nao.ac.jp² Max Planck Institute for Astronomy, Königstuhl 17, D-69117 Heidelberg, Germany³ University Observatory, Faculty of Physics, Ludwig-Maximilians-Universität München, Scheinerstr. 1, D-81679 Munich, Germany⁴ Exzellenzcluster ORIGINS, Boltzmannstr. 2, D-85748 Garching, Germany

Received 2021 April 1; revised 2021 May 28; accepted 2021 May 28; published 2021 June 22

Abstract

Recent millimeter and infrared observations have shown that gap- and ring-like structures are common in both dust thermal emission and scattered light of protoplanetary disks. We investigate the impact of the so-called thermal wave instability (TWI) on the millimeter and infrared scattered light images of disks. We perform 1+1D simulations of the TWI and confirm that the TWI operates when the disk is optically thick enough for stellar light, i.e., small-grain-to-gas mass ratio of $\gtrsim 0.0001$. The midplane temperature varies as the waves propagate, and hence gap and ring structures can be seen in both millimeter and infrared emission. The millimeter substructures can be observed even if the disk is fully optically thick since it is induced by the temperature variation, while density-induced substructures would disappear in the optically thick regime. The fractional separation between TWI-induced ring and gap is $\Delta r/r \sim 0.2\text{--}0.4$ at $\sim 10\text{--}50$ au, which is comparable to those found by the Atacama Large Millimeter/submillimeter Array. Due to the temperature variation, snow lines of volatile species move radially and multiple snow lines are observed even for a single species. The wave propagation velocity is as fast as ~ 0.6 au yr⁻¹, which can be potentially detected with a multiepoch observation with a time separation of a few years.

Unified Astronomy Thesaurus concepts: [Protoplanetary disks \(1300\)](#); [Planet formation \(1241\)](#)

Supporting material: animation

1. Introduction

The recent Atacama Large Millimeter/submillimeter Array (ALMA) observations have revealed that axisymmetric gap and ring structures are common in the dust continuum emission of protoplanetary disks (Andrews et al. 2018). The origin of these structures is still unclear, but several formation mechanisms have been proposed such as dust filtering associated with a planet-induced gap (e.g., Pinilla et al. 2012; Dipierro et al. 2015), snow lines (Zhang et al. 2015; Okuzumi et al. 2016; Pinilla et al. 2017), instability induced by dust-gas interaction (Takahashi & Inutsuka 2014, 2016), or magnetohydrodynamical effects (Flock et al. 2015; Ruge et al. 2016; Krapp et al. 2018; Riols et al. 2020). Although most of these mechanisms produce substructures via the density variation, the observed substructures have been detected even at wavelengths where the disk is fully optically thick (e.g., Carrasco-González et al. 2019; Macias et al. 2021).

The recent infrared observations have shown that the gap- and ring-like structures are also common in scattered light images (Avenhaus et al. 2018; Garufi et al. 2018). Although it is unclear if the substructures in scattered light are associated with the (sub)millimeter substructures, the prevalence of substructures in both dust and gas disks raises the following questions: how are these substructures created and how are they associated with the formation of planets?

One of the potential mechanisms that creates ring and gap structures in scattered light images is the so-called thermal wave instability (TWI; D'Alessio et al. 1999; Dullemond 2000; Watanabe & Lin 2008; Siebenmorgen & Heymann 2012; Ueda et al. 2019). The TWI is a physical instability induced at the surface of passively heated disks. If the disk surface is perturbed and a small bump is generated, the illuminated

frontside of the bump receives more stellar light and the shadowed outer side of the bump receives insufficient flux. At the illuminated side, the disk surface puffs up further as the midplane temperature increases, resulting in a further decrease in the temperature at the backside. Since the heating efficiency depends on the grazing angle, which is defined as the angle between the incident stellar light and the disk surface, the bump responsible for increasing the grazing angle moves inward and the next bump is generated just behind the former one (Figure 1).

In this Letter, we propose the TWI as a new formation mechanism of the gap and ring structures in dust millimeter continuum emission as well as the scattered light emission. We perform 1+1D simulations of the TWI and demonstrate that the TWI can be a potential origin of the observed gap and ring structures in both millimeter and infrared images. The simulation model is described in Section 2. The simulated results are shown in Section 3. A discussion and our conclusion are provided in Sections 4 and 5.

2. Model

2.1. The TWI Simulations

We perform time-dependent simulations of the TWI following a model given by Watanabe & Lin (2008). We solve a 1+1D energy equation for an axially symmetric disk. The midplane temperature T_m of a passively heated disk is calculated with the energy equation

$$\frac{\gamma + 1}{2(\gamma - 1)} \frac{k_B \Sigma_g}{\mu m_H} \frac{\partial T_m}{\partial t} = 2(F_s - F_m + F_e), \quad (1)$$

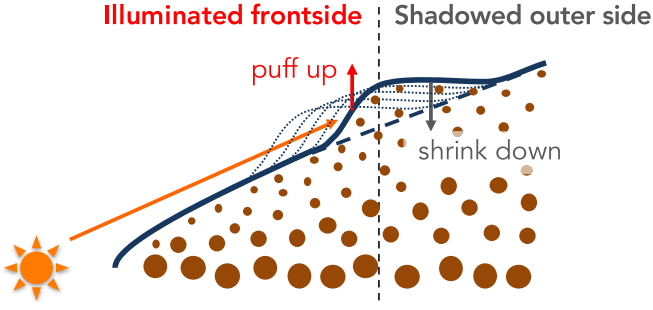


Figure 1. Schematic view of the thermal wave instability. The frontside of the perturbed disk surface receives more stellar flux and puffs up, while the shadowed outer side shrinks down (solid line). The perturbation propagates inward as a thermal wave (dotted lines).

where $\gamma = 1.4$ is the adiabatic index, k_B is the Boltzmann constant, $\mu = 2.34$ is the molecular weight of disk gas, m_H is the atomic mass unit, and Σ_g is the gas surface density. The three fluxes, F_s , F_m , and F_e , represent the incident stellar flux, released energy emitted from dust, and incident external flux, respectively, and are written as

$$F_s(r) = \{1 - \exp(-2\tau_m(T_s))\} \frac{L_*}{8\pi} \left\langle \frac{A_s}{r^2} + \frac{4R_*}{3\pi r^3} \right\rangle, \quad (2)$$

$$F_m(r) = \{1 - \exp(-2\tau_m(T_m))\} \sigma T_m^4, \quad (3)$$

$$F_e(r) = \{1 - \exp(-2\tau_m(T_m))\} \sigma T_e^4, \quad (4)$$

where R_* and L_* are the stellar radius and luminosity, respectively, T_s is the temperature of the superheated dust grains at the disk surface, and σ is the Stefan–Boltzmann constant. Following Watanabe & Lin (2008), we set the stellar parameters as $R_* = 2.08R_\odot$, $M_* = 1M_\odot$, and $T_* = 4000$ K, resulting in $L_* = 1L_\odot$. The effective temperature associated with the external heating is set as $T_e = 10$ K. The total emitting area filling factor of superheated dust grains, A_s , can be written as

$$A_s(r) = 1 - \exp \left[- \int_{z_s(r)}^{\infty} \kappa_s(T_*) \rho_d(r, z') dz' \right], \quad (5)$$

where z_s is the height of the disk surface where the radial optical depth for the stellar light reaches unity, $\kappa_s(T_*)$ is the Planck mean opacity using the stellar temperature to determine the blackbody radiation. A_s is sometimes approximated with $\sin \alpha$, where α is the grazing angle, but we follow the more accurate determination, see Appendix C in Watanabe & Lin (2008). The dust density distribution $\rho_d(r, z)$ is given by

$$\rho_d(r, z) = \frac{\Sigma_d}{\sqrt{2\pi} h_d} \exp \left(- \frac{z^2}{2h_d^2} \right), \quad (6)$$

where h_d is the scale height of the dust disk, which contributes to the opacity and is assumed to be the same as the gas scale height $h_g = \sqrt{k_B T_m r^3 / \mu m_H G M_*}$.

Equation (6) is based on an assumption that the disk is in hydrostatic equilibrium in the vertical direction. This assumption is valid when the dynamical timescale Ω_K^{-1} is shorter than

the thermal timescale given by

$$t_{\text{th}} = \frac{\gamma + 1}{2(\gamma - 1)} \frac{k_B \Sigma_g}{\mu m_H \sigma T_m^3}. \quad (7)$$

While the dynamical timescale increases as $r^{3/2}$, the thermal timescale is constant when $\Sigma_g \propto r^{-3/2}$ and $T_m \propto r^{-1/2}$. Therefore, the assumption of hydrostatic would be broken at the outer region ($\gtrsim 50$ au). However, we focus mainly on the intermediate region (~ 10 – 50 au), where the TWI operates and hence we assume the hydrostatic equilibrium for the entire region of the disk.

Using the dust distribution given by Equation (6), the vertical optical depth for the dust thermal emission is calculated as

$$\tau_m(T_m; r) = \int_0^{z_s(r)} \kappa_m(T_m) \rho_d(r, z') dz', \quad (8)$$

where $\kappa_m(T_m)$ is the Planck mean opacity for the dust emission. We consider the effects of oblique radiative transfer in a similar manner as that used in Watanabe & Lin (2008): the angle brackets on the right-hand side of Equation (2) represent a radial average of radiation emitting from surface dust with a weight of $\exp\{-(r - r')/z_s(r)\}^2$, where r' is the radial position of the emitting surface dust. This mimics the radial energy diffusion and stabilizes the disk against short-wavelength perturbations. For the opacity per unit dust mass, we assume $\kappa_* = 800 \text{ cm}^2 \text{ g}^{-1}$ and $\kappa_m = 400 \text{ cm}^2 \text{ g}^{-1}$. The adopted κ_* is based on the opacity of compact dust with the MRN distribution from 0.1 to 30 μm and a composition of 20% water ice, 33% pyroxene, 40% organics, and 7% troilite. Even though κ_m depends on the dust temperature, we assume κ_m to be constant for the entire region of the disk for simplicity.

We use the two-dimensional cylindrical coordinate (r, θ) , where r is the midplane radial distance from the central star and θ is the angle from the midplane. The calculation domain ranges from 0.03 to 300 au for the radial direction and from 0 to $\pi/6$ for the θ direction, where $\theta = 0$ corresponds to the midplane. The radial grid is logarithmically divided into 240 bins and the θ grid is linearly divided into 360 bins.

For the disk model, we use a simple power-law gas surface density with an exponential tail, $\Sigma_g = 1700(r/\text{au})^{-3/2} \exp(-r/r_d) \text{ g cm}^{-2}$, where r_d is set to be 100 au. The dust surface density is given as $f_{d2g, s} \Sigma_g$, where $f_{d2g, s}$ represents the dust-to-gas mass ratio of small grains, which contribute to the opacity. During the simulations, the gas and dust surface density is fixed, while the temperature structure and vertical height of the disk evolve. This is justified when the viscous evolution timescale of the disk is longer than the thermal timescale and is valid for this setup. For more details of the numerical procedure, we refer readers to Watanabe & Lin (2008).

2.2. Imaging Simulation

With the temperature profile obtained from the simulations, we perform radiative transfer simulations with the Monte Carlo radiative transfer code RADMC-3D (Dullemond et al. 2012) to obtain model images. In the simulation, we use two dust populations: small grains with a maximum radius of 10 μm and a dust-to-gas mass ratio of $f_{d2g, s}$ and large grains with a maximum radius of 1 mm and a dust-to-gas mass ratio of

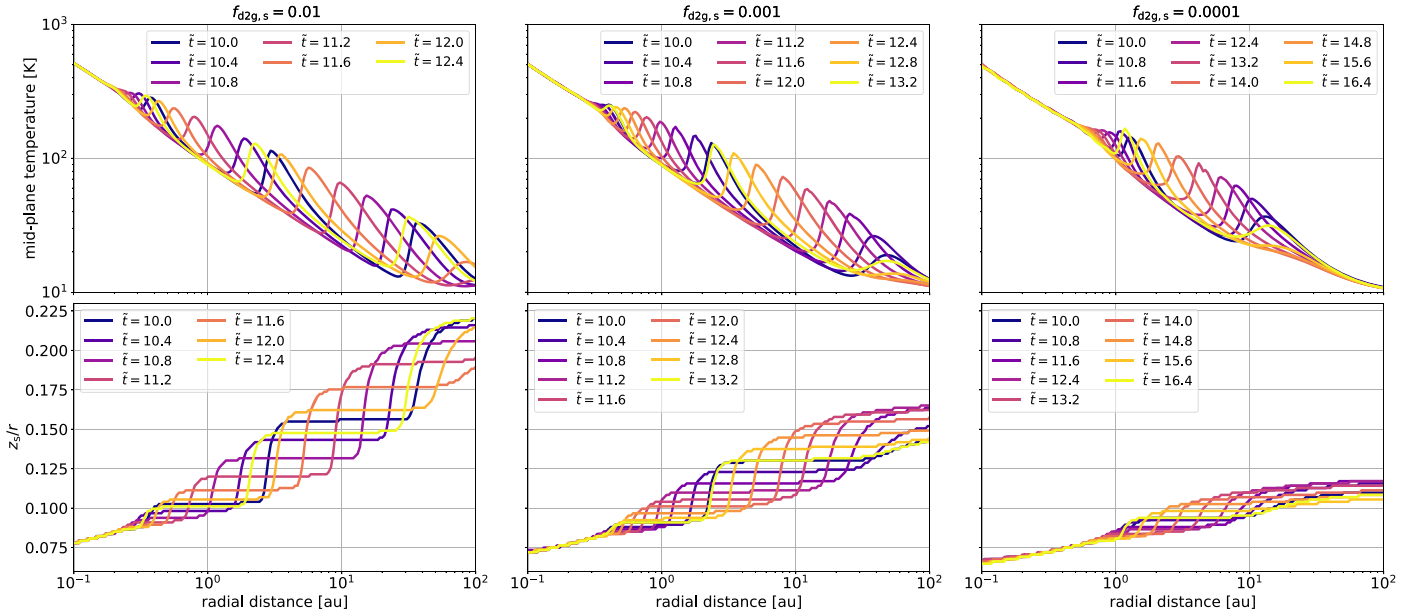


Figure 2. Time evolution of the midplane temperature (top) and the height of disk surface (bottom) for the models with $f_{d2g,s} = 0.01$ (left), 0.001 (center), and 0.0001 (right). An animated version of this figure provides the whole time evolution of the TWI from $\tilde{t} = 0$ to 19.8. (An animation of this figure is available.)

0.01– $f_{d2g,s}$. Each dust population has a differential size distribution with a power-law index of -3.5 (Mathis et al. 1977) from the minimum dust radius of $0.1 \mu\text{m}$. The small grains are assumed to be well mixed with the gas. The scale height of the large dust grains is assumed to be 10 times lower than that of the gas to mimic the effect of vertical settling. For the dust opacity we adopt the DSHARP opacity model (Birnstiel et al. 2018). The simulated images are convolved with a beam size of $0''.03$ and assuming a distance from the Earth of 140 pc.

3. Results

Figure 2 shows the time evolution of the midplane temperature and the height of the disk surface for the models with $f_{d2g,s} = 0.01$, 0.001, and 0.0001. The variable \tilde{t} denotes the time normalized by the initial thermal timescale $t_{\text{th},0} = 41.2$ yr. In all models, we clearly observe the thermal wave instability. At the illuminated frontside of the waves, the midplane temperature steeply increases with the radial distance. Along with the increase in the temperature, the starlight-absorbing surface makes a steep angle to the star’s rays and the disk surface also steeply increases. The puffed-up disk surface blocks off the stellar light and produces the shadowed outer region, where z_s/r is almost constant with the radial distance. In the shadowed region, the midplane temperature steeply decreases because of no direct stellar illumination.

In the model with $f_{d2g,s} = 0.01$, the peak of the wave located at 40 au at $\tilde{t} = 10$ moves inward and reaches 10 au at $\tilde{t} = 11.2$, which corresponds to a velocity of 0.625 au yr^{-1} . The waves move more slowly at a more inner region and finally vanish at $\lesssim 0.3$ au. The propagation velocity is roughly equivalent to r/t_{th} when $f_{d2g,s} = 0.01$ but also depends on $f_{d2g,s}$; the wave velocity at 10 au is 0.25 au yr^{-1} ($\approx 4 \times 10^{-3} v_K$) for $f_{d2g,s} = 0.01$, 0.24 au yr^{-1} ($\approx 3.8 \times 10^{-3} v_K$) for $f_{d2g,s} = 0.001$ and 0.14 au yr^{-1} ($\approx 2.2 \times 10^{-3} v_K$) for $f_{d2g,s} = 0.0001$. We expect that this dependence would be connected with the height of the absorption surface. The height of the absorption surface weakly

depends on the dust surface density and decreases as $z_s \propto \sqrt{\log \Sigma_d}$ (Muto 2011). This decreasing trend in z_s can be seen in the bottom panels of Figure 2. The propagation velocity is expected to be related to the rate of change in the vertical position of the absorption surface $\partial z_s / \partial t$, which would be proportional to z_s . Since larger $f_{d2g,s}$ yields larger z_s , the propagation velocity would also be larger for larger $f_{d2g,s}$.

For the model with $f_{d2g,s} = 0.01$, the midplane temperature oscillates with a timescale of $\sim 2.4 t_{\text{th},0} \approx 99$ yr. The oscillation timescale is longer for smaller $f_{d2g,s}$: $\sim 3.2 t_{\text{th},0} \approx 132$ yr for $f_{d2g,s} = 0.001$ and $\sim 6.4 t_{\text{th},0} \approx 264$ yr for $f_{d2g,s} = 0.0001$. This trend is more clearly shown in Figure 3. Figure 3 shows the midplane temperature at 5 and 50 au for the models with $f_{d2g,s} = 0.01$, 0.001, and 0.0001. At 5 au, the midplane temperature varies from ~ 30 K to ~ 80 – 90 K for all models. The time separation of each peak is larger for smaller $f_{d2g,s}$. This is because smaller $f_{d2g,s}$ makes the disk more stable for the TWI. As the radial length scale over which the stellar radiation is absorbed, i.e., the thickness of the absorption layer for the stellar light, is longer for smaller $f_{d2g,s}$ (Appendix B), smaller $f_{d2g,s}$ is stable for longer wavelength perturbations. Since the growth rate of the perturbation is inversely proportional to the wavelength (Dullemond 2000), the TWI grows more slowly for smaller $f_{d2g,s}$.

The radial extent on which the TWI operates also depends on $f_{d2g,s}$ and is broader for larger $f_{d2g,s}$. While for $f_{d2g,s} = 0.01$, the radial extent of TWI activity is between 0.3 and 100 au, this extent shrinks for $f_{d2g,s} = 0.0001$ to the region between 1 and 10 au. The inner edge of the unstable region is set by the irradiation from the central star with a finite radius (D’Alessio et al. 1999). Since the lower $f_{d2g,s}$ disk has a starlight-absorbing surface closer to the midplane, the finite size of the central star has a bigger effect on the lower $f_{d2g,s}$ disk. It is worth noting that the TWI can also be suppressed at the inner region by the accretion heating, which is ignored in our simulations (Watanabe & Lin 2008). At the outer region, the disk is stable for the TWI because the external irradiation suppresses the

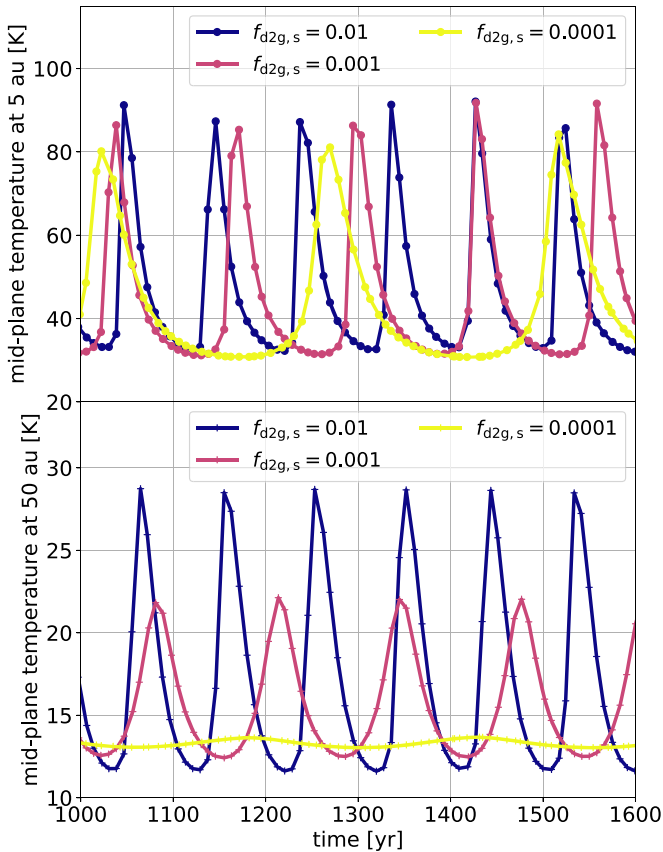


Figure 3. Time evolution of the midplane temperature at 5 au (top) and 50 au (bottom) for $f_{d2g,s} = 0.01, 0.001,$ and 0.0001 .

growth of the TWI. Since the smaller $f_{d2g,s}$ makes the disk thinner and hence cooler, the TWI can grow only at the more inner region for smaller $f_{d2g,s}$. At 50 au, we clearly see that the amplitude of the temperature variation decreases with $f_{d2g,s}$ and almost vanishes when $f_{d2g,s} = 0.0001$. This trend indicates that the TWI can produce the rings and gaps when the disk contains a large enough amount of small dust grains.

Figure 4 shows the face-on view of the TWI-operated disk at infrared wavelength ($\lambda = 1.65 \mu\text{m}$) and millimeter wavelength ($\lambda = 870 \mu\text{m}$ and 3.1 mm). The simulated images are convolved with a beam size of $0''.03$, which is comparable to the resolution of recent ALMA survey studies. Both in scattered light and dust continuum images, an inner disk component with a bright ring separated with a gap at $\sim 10\text{--}15 \text{ au}$ is clearly detected. Importantly, since the millimeter substructures are caused by the temperature variation, the substructures are visible regardless of whether the disk is optically thin or thick for its own thermal emission. We observe the ring structure at almost the same place at all wavelengths. The width of the gap is also almost the same at all wavelengths, but the local minimum has a slight radial offset between the scattered light and millimeter images. This is because the millimeter emission reflects the dust temperature, which has a local minimum at the outer edge of the shadowed region, while the scattered light images reflect the shape of the disk surface, which is almost flat in the shadowed region (Figure 2). At millimeter wavelengths, the intensity contrast between the ring and gap is ~ 3 , while it is more pronounced, $\sim 10^3$, at the infrared wavelength. The separation of the gap and ring, Δr , is typically $\sim 0.2\text{--}0.4 r_{\text{gap}}$, where r_{gap} is the radial position of the

gap, which is comparable to or slightly larger than the typical observed ones (Appendix A).

4. Discussion

4.1. Locations of Snow Lines

Snow lines of abundant volatile species are one of the possible origins of the observed substructures in dust continuum emission (Zhang et al. 2015; Okuzumi et al. 2016; Pinilla et al. 2017). Recent disk surveys have shown that the locations of the observed gap/ring structures do not seem to be related to the radial locations of the snow lines (Huang et al. 2018; Long et al. 2018; van der Marel et al. 2019). To estimate the positions of the snow lines in observed disks, the temperature profile is often assumed to be a simple power law (Huang et al. 2018; Long et al. 2018), which is broken if the disk has shadows on the disk surface (Dullemond et al. 2001; Baillié & Charnoz 2014; Ueda et al. 2019). Figure 5 shows the radial positions of snow lines of H_2O , NH_3 , CO_2 , H_2S , C_2H_6 , CH_4 , and CO at $\tilde{t} = 0$ and 11. For simplicity, we define the snow lines as the radial location where the midplane temperature reaches 150, 70, 55, 50, 40, 25, and 20 K for H_2O , NH_3 , CO_2 , H_2S , C_2H_6 , CH_4 , and CO , respectively. We clearly see that the radial positions of snow lines move with time and multiple snow lines emerge even for a single species. This means that it is necessary to determine the disk temperature precisely when we evaluate the snow line locations. These snow lines would induce additional ring and gap structures and some of them would overlap with the TWI-induced substructures. It should be noted that the oscillation timescale of the TWI is much shorter than the dust radial drift timescale. Therefore, sintering-induced substructures would not coincide with the locations of the snow lines if the TWI is present. However, the dust-size variation can be induced by sublimation and recondensation, which potentially produces millimeter substructures. Since the radial locations of the snow lines are important not only for the substructure formation but also for the chemical composition of forming planets (e.g., Sato et al. 2016; Öberg & Wordsworth 2019), we should investigate how the TWI evolves in planet forming disks.

4.2. Characteristics of TWI-induced Rings and Gaps

In this section we summarize the characteristics of the TWI-induced rings/gaps and discuss how we can distinguish the TWI from the other substructure formation mechanisms. The key points of the TWI-induced gap and ring structure are as follows.

1. The intensity variation is induced by the temperature variation (i.e., variation in the gas scale height), not surface density variation. Therefore, the substructures are visible even if the disk is fully optically thick at millimeter wavelengths. The density-induced substructures at millimeter wavelengths would be invisible if the disk is fully optically thick. Furthermore, even inside and within the TWI-induced gap can be filled with dust grains, while a planet-induced gap would trap large grains at the outer edge of the gap and the inner region should be depleted in large dust. Multiwavelength millimeter observations would be helpful to distinguish the temperature-induced intensity variation from the density-induced one.

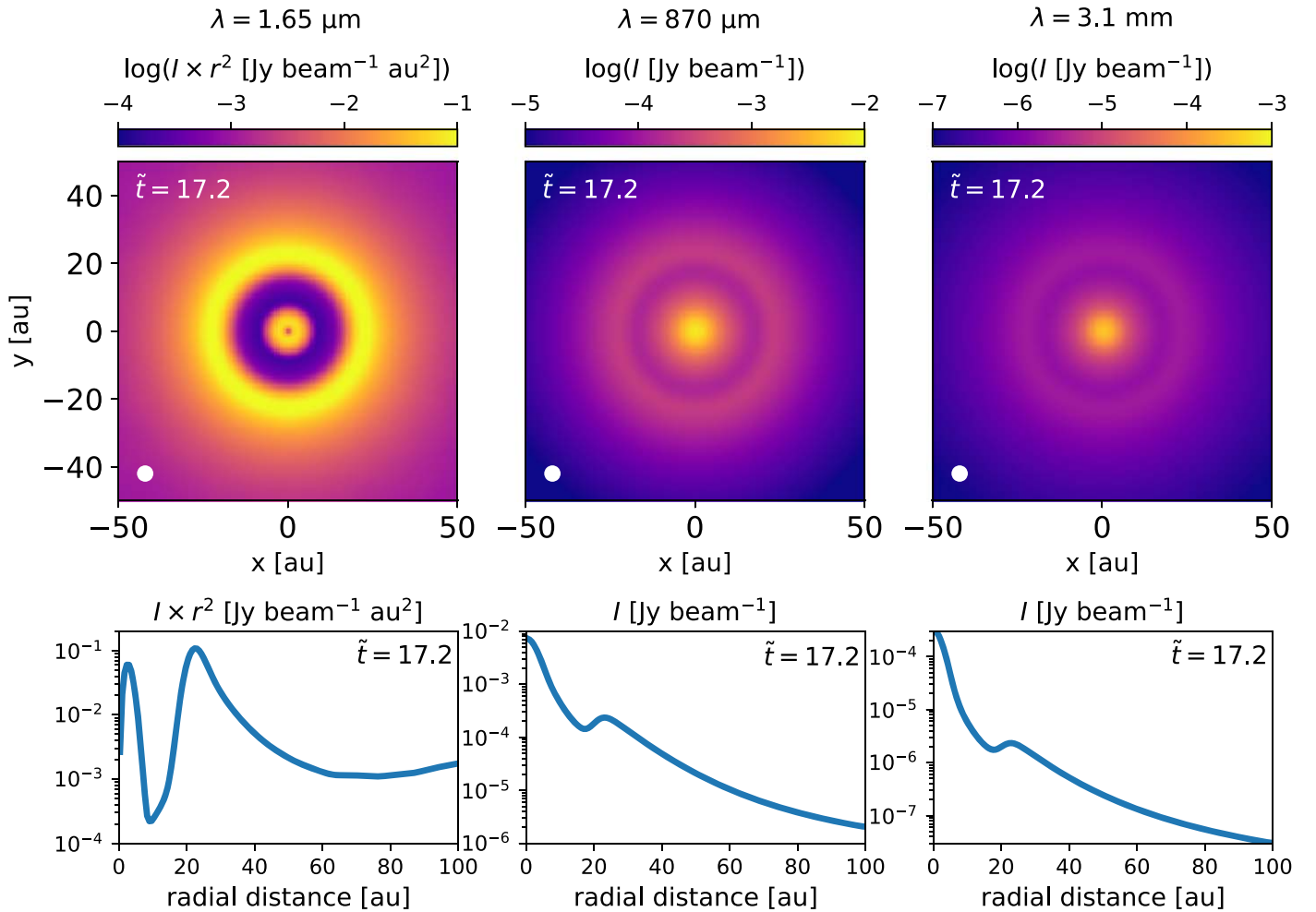


Figure 4. Synthesized images of the thermal wave instability observed at $\lambda = 1.65 \mu\text{m}$ (left), $870 \mu\text{m}$, and 3.1 mm for the model with $f_{\text{d2g,s}} = 0.01$. The images are convolved with a beam size of $0''.03$, which is denoted with a filled white circle at the bottom left in each panel. The simulated intensity at $\lambda = 1.65 \mu\text{m}$ is multiplied by a square of the radial distance to compensate for the stellar flux attenuation.

2. The gap and ring move inward as fast as a velocity of $\sim 0.6 \text{ au yr}^{-1}$, depending on the disk optical depth and the radial position. Multiepoch observations with a time separation of a few years can potentially detect the radial motion of the wave. The substructures induced by the other mechanisms would move more slowly. For example, substructures associated with a planet-induced gap would migrate with a velocity slower than the type I migration (e.g., Kanagawa et al. 2018).
3. The gap and ring structure should appear both in millimeter dust continuum and infrared scattered light. The intensity variation is more pronounced for the scattered light. The other mechanisms also potentially produce substructures in both since the distribution of small grains would be closely related to that of large grains if collisional fragmentation takes place (e.g., Pinilla et al. 2015).
4. The fractional separation between the ring and gap is typically $\Delta r/r \sim 0.2\text{--}0.4$. The other mechanisms, e.g., snow lines, might produce additional substructures between the TWI-induced ring and gap, which makes the apparent separation smaller.

4.3. Caveats

Here we summarize our assumptions and discuss the potential effect on the TWI. First, we assumed that the disk is in hydrostatic equilibrium in the vertical direction. This assumption would be broken in the outer region ($>50 \text{ au}$). The hydrodynamical motion of the disk gas might potentially suppress the TWI at the outer region, although its effect is very uncertain. Second, we fixed the gas and dust surface densities during the TWI simulations. Since the TWI is closely related to the disk optical depth for the stellar light, surface density evolution affects the behavior of the TWI. However, as shown, the evolution timescale of the TWI is very fast and much shorter than the typical viscous evolution timescale. Therefore, the assumption of fixed gas surface density would be justified. Even though the TWI might affect the dust surface density through the steep positive temperature gradient, which traps the radially drifting dust particles, the wave propagation timescale is too fast compared to the radial drift timescale. We compare these timescales in Appendix C. Finally, we treat the disk with a 1+1D approach that mimics oblique radiative transfer but ignore the radial heat diffusion and the hydrodynamical motion of the gas. The steep radial gradient in the temperature might induce the radial motion of the disk gas, which potentially suppresses the TWI. The two-dimensional radiation

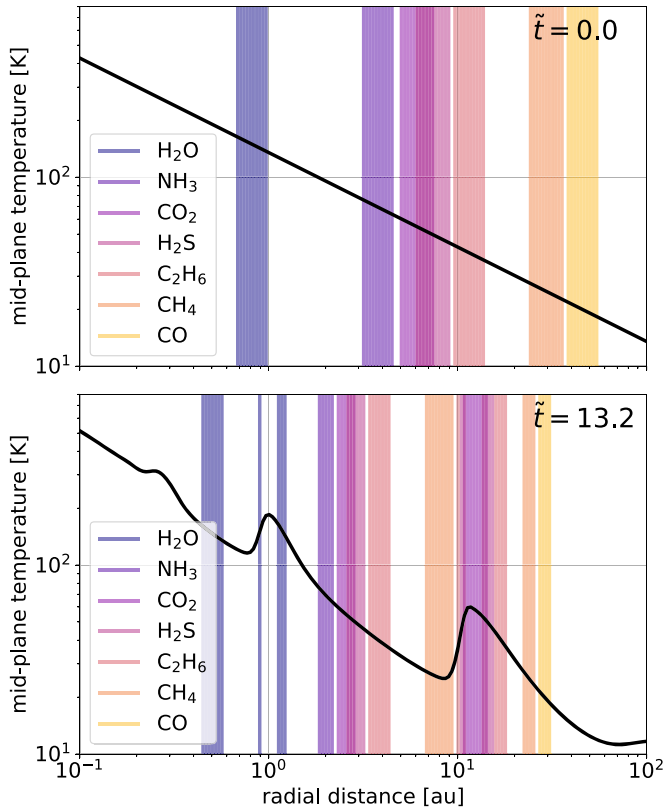


Figure 5. Radial locations of the snow lines of volatile species at $\tilde{t} = 0$ and 11 for $f_{d2g,s} = 0.01$.

hydrodynamical simulation would be necessary to investigate the TWI in more detail, taking these effects into account.

5. Summary

We investigated the impact of the thermal wave instability (TWI) on the millimeter and infrared emission of disks using the 1+1D simulations of disk temperature evolution. We confirm that the TWI operates when the disk is optically thick enough for stellar light, i.e., the dust-to-gas mass ratio of small grains is $\gtrsim 0.0001$. The midplane temperature varies as the waves propagate and hence gap and ring structures can be seen in both millimeter and infrared emission even if the dust and gas surface density have no substructures. Since the substructures are induced by the temperature variation, the millimeter substructures can be seen even if the disk is completely optically thick, while the density-induced substructures would disappear for optically thick disks. The fractional separation between the TWI-induced ring and gap is typically ~ 0.2 – 0.4 at ~ 10 – 50 au, although additional substructures might form within them, e.g., by snow lines. Due to the temperature variation, snow lines of volatile species move radially and multiple snow lines are observed even for a single species, which would affect the disk chemistry. The wave propagation velocity is as fast as ~ 0.6 au yr $^{-1}$, which can be potentially detected with a multipoint observation with a time separation of a few years. The TWI might be stabilized by the radial energy diffusion and/or hydrodynamical motion of the disk gas, which are not fully taken into account in this work. The two-dimensional radiation hydrodynamical simulation should be carried out to understand how the TWI evolves in planet forming disks.

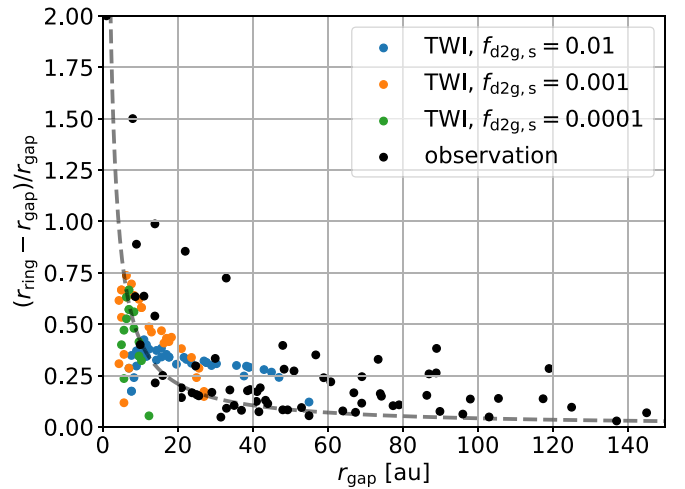


Figure 6. Fractional separation of observed and simulated gap and ring pairs. The observational data is compiled from Huang et al. (2018) and Long et al. (2018) (see also Andrews 2020). The gray dashed line denotes the condition for the ring-gap separation to be equivalent to the spatial resolution corresponding to an angular resolution of $0''.03$ assuming the distance from the Earth of 140 pc, i.e., $\Delta r = 4.2$ au.

We thank an anonymous referee for the constructive feedback. This work is supported by JSPS KAKENHI Grant Numbers JP19J01929. T.B. acknowledges funding from the European Research Council (ERC) under the European Union’s Horizon 2020 research and innovation program under grant agreement No. 714769 and funding by the Deutsche Forschungsgemeinschaft (DFG, German Research Foundation) under Germany’s Excellence Strategy—EXC-2094-390783311.

Software: RADMC-3D (Dullemond et al. 2012).

Appendix A

Comparison with the Observed Substructures

In this appendix, we compare the separation of simulated ring and gap pairs with that found by ALMA surveys. Figure 6 shows observed and simulated separation of ring and gap pairs Δr normalized by the radial location of the gap r_{gap} . The simulated fractional separation is calculated from the model images at ALMA Band 7 ($\lambda = 870$ μm), while the observations are at ALMA Band 6 ($\lambda = 1.3$ mm). Although the observing wavelength is different between the model and observation, the fractional separation of the TWI-induced ring and gap is not so sensitive to the observing wavelength since it is induced by the temperature. The observed fractional separation is typically < 0.5 at > 40 au and shows an increasing trend with decreasing the radial distance. At the intermediate disk region (~ 10 – 50 au), the fractional separation of the TWI-induced ring and gap pairs is ~ 0.2 – 0.4 , which is comparable or slightly higher than the observed values. At the outer region ($\gtrsim 50$ au), the substructures are found in the observations but are not seen in the simulations with our setup. The substructures at the outer region are potentially induced by the TWI if the disk is more massive and the central star is more luminous than our model. At the inner region ($\lesssim 10$ au), the TWI can produce ring and gap pairs with $\Delta r/r \lesssim 0.75$, though most of them are not easy to detect with the current ALMA resolution. It should be noted that the origin of the rings and gaps would not be identical but multiple formation mechanisms would take place. If multiple mechanisms take place in a disk, the ring and gap pairs induced

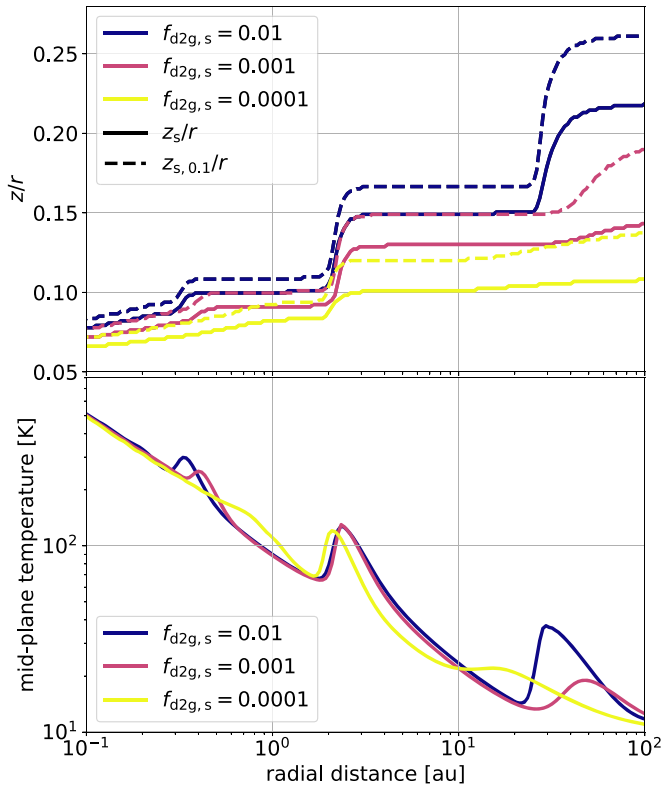


Figure 7. Top: vertical positions where the radial optical depth for the stellar light reaches 0.1 ($z_{s,0.1}$; dashed lines) and 1 (z_s ; solid lines) for different values of $f_{d2g,s}$. Bottom: midplane temperature profile for different values of $f_{d2g,s}$.

by each mechanism might be overlapped. If this is the case, the apparent separation of gap and ring pairs would be smaller than the original.

Appendix B The Height of Disk Surface

Figure 7 shows the vertical locations where the radial optical depth for the stellar light reaches 0.1 ($z_{s,0.1}$) and 1 (z_s) for different values of $f_{d2g,s}$. For each model, we plot a time snapshot where the wave is located at a similar location (~ 25 au) to compare the surface structure clearly. We see that the absorption surface is located lower for smaller $f_{d2g,s}$. The vertical thickness of the absorption layer, i.e., the region where the optical depth ranges from ~ 0.1 to 1, Δz_s , slightly increases as $f_{d2g,s}$ decreases. As z_s decreases with $f_{d2g,s}$, the thickness-to-height ratio, $\Delta z_s/z_s$, increases with decreasing $f_{d2g,s}$ more sensitively. Since the longest wavelength of perturbations is an order of $\sim z_s$ and perturbations with a wavelength shorter than Δz_s is expected to be suppressed, larger $\Delta z_s/z_s$ would make the disk stable for perturbations with longer wavelengths. This means that smaller $f_{d2g,s}$ is more stable for the TWI. The larger $f_{d2g,s}$ has a larger vertical gap in z_s at ~ 25 au but the temperature variation is similar for all models. This is because the midplane temperature is more sensitive to the radial gradient of the disk surface than the absolute height.

Appendix C Comparison of Physical Timescales

In this appendix, we compare the thermal timescale, viscous evolution timescale, dust radial drift timescale, and disk dynamical timescale in Figure 8. The thermal timescale is

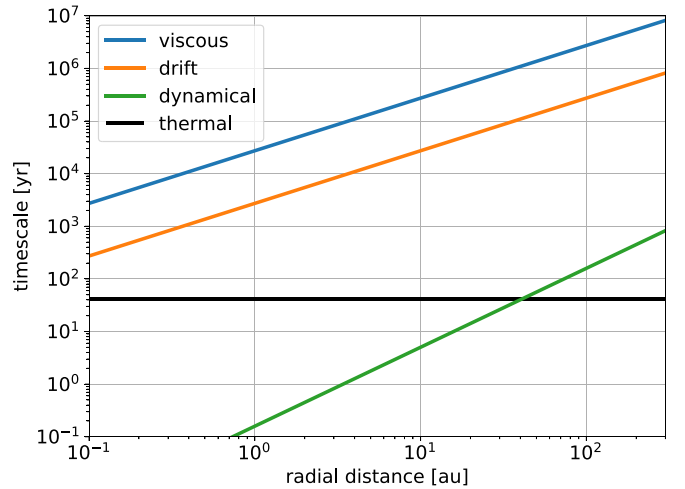


Figure 8. Comparison of the viscous evolution timescale (blue), dust radial drift timescale (orange), dynamical timescale (green), and thermal timescale (black).

41.2 yr and independent of the radial distance for our setup in the optically thick limit (Equation (7)). The viscous evolution timescale t_{vis} is estimated as $t_{\text{vis}} = r^2/\alpha c_s h_g$, where α is the viscosity parameter. We adopt $\alpha = 10^{-2}$ and a simple power-law temperature profile of $150(r/\text{au})^{-0.5}$ K. Using these, the viscous evolution timescale is estimated as $2.8 \times 10^4 (r/\text{au})$ yr. We clearly see that the viscous evolution timescale is much longer than the thermal timescale. The radial drift timescale of dust grains t_{drift} is evaluated as $t_{\text{drift}} = r/v_d$, where v_d is the radial drift velocity. The radial drift velocity is given as $\eta \text{St} v_K$, where $\eta = 0.5(c_s/v_K)^2 d \ln p/d \ln r$ and St is the normalized stopping time of dust grains. We adopt $\text{St} = 0.1$ and obtained $t_{\text{drift}} = 2.8 \times 10^3 (r/\text{au})$ yr. The dust radial drift timescale is much shorter than the viscous evolution timescale but much longer than the thermal timescale. The dynamical timescale t_{dyn} is defined as $t_{\text{dyn}} = \Omega_K^{-1} = 0.16 (r/\text{au})^{1.5}$. The dynamical timescale is much shorter than the thermal timescale at $r \lesssim 40$ au but longer at the outer region.

ORCID iDs

Takahiro Ueda <https://orcid.org/0000-0003-4902-222X>
 Mario Flock <https://orcid.org/0000-0002-9298-3029>
 Tilman Birnstiel <https://orcid.org/0000-0002-1899-8783>

References

- Andrews, S. M. 2020, *ARA&A*, 58, 483
 Andrews, S. M., Huang, J., Pérez, L. M., et al. 2018, *ApJL*, 869, L41
 Avenhaus, H., Quanz, S. P., Garufi, A., et al. 2018, *ApJ*, 863, 44
 Baillié, K., & Charnoz, S. 2014, *ApJ*, 786, 35
 Birnstiel, T., Dullemond, C. P., Zhu, Z., et al. 2018, *ApJL*, 869, L45
 Carrasco-González, C., Sierra, A., Flock, M., et al. 2019, *ApJ*, 883, 71
 D’Alessio, P., Cantó, J., Hartmann, L., Calvet, N., & Lizano, S. 1999, *ApJ*, 511, 896
 Dipierro, G., Price, D., Laibe, G., et al. 2015, *MNRAS*, 453, L73
 Dullemond, C. P. 2000, *A&A*, 361, L17
 Dullemond, C. P., Dominik, C., & Natta, A. 2001, *ApJ*, 560, 957
 Dullemond, C. P., Juhasz, A., Pohl, A., et al. 2012, RADMC-3D: A Multi-purpose Radiative Transfer Tool, Astrophysics Source Code Library, ascl:1202.015
 Flock, M., Ruge, J. P., Dzyurkevich, N., et al. 2015, *A&A*, 574, A68
 Garufi, A., Benisty, M., Pinilla, P., et al. 2018, *A&A*, 620, A94
 Huang, J., Andrews, S. M., Dullemond, C. P., et al. 2018, *ApJL*, 869, L42
 Kanagawa, K. D., Tanaka, H., & Szuszkiewicz, E. 2018, *ApJ*, 861, 140
 Krapp, L., Gressel, O., Benítez-Llambay, P., et al. 2018, *ApJ*, 865, 105

- Long, F., Pinilla, P., Herczeg, G. J., et al. 2018, [ApJ](#), **869**, 17
- Macias, E., Guerra-Alvarado, O., Carrasco-Gonzalez, C., et al. 2021, [A&A](#), **648**, A33
- Mathis, J. S., Rimpl, W., & Nordsieck, K. H. 1977, [ApJ](#), **217**, 425
- Muto, T. 2011, [ApJ](#), **739**, 10
- Öberg, K. I., & Wordworth, R. 2019, [AJ](#), **158**, 194
- Okuzumi, S., Momose, M., Sirono, S.-i., Kobayashi, H., & Tanaka, H. 2016, [ApJ](#), **821**, 82
- Pinilla, P., Benisty, M., & Birnstiel, T. 2012, [A&A](#), **545**, A81
- Pinilla, P., de Juan Ovelar, M., Ataiee, S., et al. 2015, [A&A](#), **573**, A9
- Pinilla, P., Pohl, A., Stammerl, S. M., & Birnstiel, T. 2017, [ApJ](#), **845**, 68
- Riols, A., Lesur, G., & Menard, F. 2020, [A&A](#), **639**, A95
- Ruge, J. P., Flock, M., Wolf, S., et al. 2016, [A&A](#), **590**, A17
- Sato, T., Okuzumi, S., & Ida, S. 2016, [A&A](#), **589**, A15
- Siebenmorgen, R., & Heymann, F. 2012, [A&A](#), **539**, A20
- Takahashi, S. Z., & Inutsuka, S.-i. 2014, [ApJ](#), **794**, 55
- Takahashi, S. Z., & Inutsuka, S.-i. 2016, [AJ](#), **152**, 184
- Ueda, T., Flock, M., & Okuzumi, S. 2019, [ApJ](#), **871**, 10
- van der Marel, N., Dong, R., di Francesco, J., Williams, J. P., & Tobin, J. 2019, [ApJ](#), **872**, 112
- Watanabe, S.-i., & Lin, D. N. C. 2008, [ApJ](#), **672**, 1183
- Zhang, K., Blake, G. A., & Bergin, E. A. 2015, [ApJL](#), **806**, L7